

Nucleate Pool Boiling of R-245fa at Low Saturation Temperatures for Hydrogen Precooling Applications

Gilberto Moreno*, Bidzina Kekelia, Hariswaran Sitaraman, Sreekant Narumanchi, Kevin Bennion

National Renewable Energy Laboratory
15013 Denver West Parkway
Golden, CO 80401-3305

*corresponding author contact details:

email: gilbert.moreno@nrel.gov

phone: 303-275-4450

Abstract

Experiments were conducted to measure the pool boiling performance of saturated R-245fa at low saturation temperatures (-30°C, -40°C, and -50°C). Horizontally oriented cylindrical heat sources were used as the test samples and were intended to simulate a small section of a hydrogen-filled tube. Measurements evaluated the effects of saturation temperature and two microporous coatings on heat transfer coefficients (HTC), critical heat flux (CHF), and boiling incipient superheat. Results show that boiling performance decreases as the saturation temperature reduces—a result of less active nucleation sites and higher vapor coverage of the heated surface at lower temperatures. Microporous coatings increased HTCs and CHF values, but did not have a significant effect on reducing the boiling incipient superheat. The experimental results were used to develop correlations for nucleate pool boiling on plain and microporous surfaces that can be used to predict HTCs and CHF values at low saturation temperature conditions (down to -50°C).

Keywords: CHF, hydrogen heat exchangers, low- temperature boiling, nucleate pool boiling

Declarations of interest: None

1 Introduction

Fuel cell electric vehicles are currently the only zero-tailpipe-emission vehicle technology capable of over a 300-mile range with a sub-five-minute fueling time. Fuel cell electric vehicles are commercially available today, but the hydrogen infrastructure with which to fuel them lags far behind in commercial readiness. A critical issue with current hydrogen fueling stations is the thermal management systems required to precool hydrogen to temperatures as low as -40°C [1]. Precooling of hydrogen is required to avoid exceeding the temperature limits of the vehicle's onboard storage tank during the hydrogen fueling process. Existing hydrogen precooling systems are bulky and inefficient, resulting in excessive cost to facility operators and customer inconveniences.

Two-phase (boiling) cooling provides high heat transfer capabilities with the potential to improve the thermal performance of hydrogen precooling systems. Designing a boiling-based cooling system requires information on the pool boiling heat transfer performance of refrigerants at low temperatures. A review of the available literature shows a lack of information related to boiling heat transfer at saturated temperatures below -30°C . Decreasing the fluid saturation temperatures (i.e., decreasing pressure) is well known to decrease boiling heat transfer coefficients (HTC) [2–5]. Critical heat flux (CHF) values typically achieve a maximum value at about one-third the critical pressure and decreases monotonically at either end of the peak value [3,4].

Lee and Mudawar [6,7] conducted experiments to test the thermal performance of an indirect refrigeration cooling system to enable high-heat-flux dissipation at low component temperatures. The indirect refrigeration cooling system consisted of two flow loops—an HFE-7100 pumped loop that cooled a small heat source and a vapor-compression system that cooled liquid HFE-7100 via a heat exchanger. The refrigeration system cooled HFE-7100 down to -30°C , and the highly subcooled HFE-7100 was then pumped through a microchannel cold plate to dissipate heat from a $0.5\text{ cm} \times 1\text{ cm}$ heat source. Heat dissipation in excess of $7,000\text{ kW/m}^2$ was measured using this cooling approach. It is stated that the indirect refrigeration cooling configuration is beneficial since it decouples the vapor requirements of the refrigeration system compressor (e.g., compressor typically requires superheated vapor) from the vapor requirements of the microchannel cold plate (e.g., need to stay below the CHF).

A significant amount of the available low-temperature boiling research is focused on the study of evaporators in refrigeration systems. These refrigeration-related studies typically use forced convection, are limited to lower heat fluxes ($<20\text{ kW/m}^2$), and are typically conducted at saturation temperatures between 4°C and 10°C . De Rossi et al. [8] measured the boiling HTCs of R-134a flowing within a 6-mm-diameter tube at saturation temperatures ranging from -9°C to 20°C . They report that boiling HTCs are higher at higher saturated temperatures and lower vapor qualities. Wattelet et al. [9] compared the flow boiling performance of R-12 and R-134a at saturation temperatures between -15°C and 5°C . R-134a is reported to provide HTCs that were about 25% higher than R-22 HTCs. Additionally, an HTC correlation was developed that provided a good match to their experimental data. Thome [10] conducted an extensive literature review detailing the flow boiling performance of various refrigerants at saturation temperatures as low as -21°C . The work emphasized the inability of the available correlations to accurately predict thermal performance for all cases.

Pool boiling on cylindrical tubes is commonly employed as a means of cooling water in centrifugal-type chillers. Ribatski and Jabardo [11] conducted pool boiling experiments using R-11, R-123, R-12, R-134a, and R-22 on cylindrical heaters to develop an HTC correlation. Tests with R-134a were conducted at a reduced pressure ($P_{red} = P / P_c$) of 0.007 which corresponds to $T_{sat} = 0^\circ\text{C}$. Experimental conditions were varied to understand the effects of the reduced pressure, surface roughness, and heater material on HTCs. It is reported that the P_{red} and surface roughness have the biggest influence on HTCs. HTCs for different refrigerants were measured to be similar when compared at the same P_{red} . This reduced-pressure effect is consistent with what other studies have reported [5,12].

Nagata et al. [13] measured the condensation and pool boiling HTCs for R-1234ze(E), R-1234ze(Z), R-1233zd(E), R-134a, and R-245fa on smooth horizontal cylindrical heaters. Boiling experiments were conducted at saturation temperatures ranging from 10°C to 60°C with heat fluxes $<80 \text{ kW/m}^2$, and thus CHF was not measured in their study. They evaluated various HTC correlations and found that the Ribatski and Jabardo [11] correlation best matched their experimental results. Decreasing the saturation temperatures from 60°C to 10°C was found to decrease HTC. The decrease in HTC was associated with a decrease in the nucleation-site density (measured in their study) and an increase in the bubble departure size at lower saturation temperatures (i.e., lower P_{red}).

Surface enhancement techniques can be used to increase boiling heat transfer and thus can be used to compensate for lower HTCs at lower saturation temperatures. A variety of surface enhancement features have been used to increase boiling HTCs and CHF. The following is a summary of some surface enhancement techniques that have been used on cylindrical heated surfaces. Webb and Pais [12] conducted pool boiling tests using commercially available enhanced tubes (Wieland GEWA K26 and GEWA TX; Wolverine Tube Turbo-B) that consisted of millimeter-scale finned structures. The enhanced tubes were tested using R-134a as well as older-generation refrigerants at 4°C and 27°C saturation temperatures. The enhanced tubes were found to increase HTCs by over 200% as compared with the plain tube. More recently, van Rooyen and Thome [14] characterized the boiling heat transfer performance of the latest enhanced-tube products from Wolverine Tube (Turbo B5) and Wieland Werke (GEWA B5). Experiments were conducted using R-134a, R-236fa, and R-1234ze(E) at saturation temperatures ranging from 5°C to 25°C . The performance of the two tubes (Turbo B5 and GEWA B5) was stated to be similar, but their enhancement versus a baseline plain tube was not quantified. Additionally, varying the saturation temperature had minimal effect on the HTCs for both enhanced tubes. Gorgy [15] measured the pool boiling performance of low-global warming potential refrigerants including R-123ze, R-1233zd(E), and R-450A at a saturation temperature of 4.4°C . Surface enhancements were used to augment heat transfer and reported to increase HTC by almost 900%. The surface enhancements were described to be finned structures, but the finned structure geometry was not well described or imaged. The effect of the enhanced tubes on CHF was not reported for these studies [12,14,15].

Porous coatings characterized by random micrometer-scale structures with interconnected tunnels have also been used to increase boiling heat transfer. Dewangan et al. [16] measured the boiling HTC of two porous copper coatings fabricated using a thermal spraying technique. The porous coatings were tested using R-134a, R-600a, and R-410A at $T_{sat} = 10^\circ\text{C}$ and were reported to increase HTCs by as much as 80%. Hsieh and Weng [17] created porous coatings using plasma and flame spray techniques. The coatings were

fabricated on 19-mm-diameter horizontally oriented tubes and tested with R-134a and R-407c at $T_{\text{sat}}=4^{\circ}\text{C}$. The coatings were reported to increase HTC by as much as 150% as compared with a plain tube. The superheated liquid layer that surrounds the porous structures is stated to facilitate evaporation and bubble growth, resulting in higher HTCs. Additionally, the coating thickness and porosity were reported to have a bigger influence on HTCs than surface roughness. Ji et al. [18] conducted pool boiling experiments using horizontal tubes with copper foam coatings. The coatings had relatively high porosity values ($\geq 90\%$) and were brazed onto the outer diameter of the copper tubes. Experiments were conducted with R-134a at $T_{\text{sat}} = 6^{\circ}\text{C}$. The thicker coating (2.6 mm) was found to provide lower HTCs as compared to the thinner coating (1.6 mm) due to an accumulation of vapor within the thicker porous structure. CHF values were not measured for these microporous-coated tube studies [16–18].

In this study, the pool boiling performance for R-245fa was measured at low saturation temperatures of -30°C ($P_{\text{red}} = 0.003$), -40°C ($P_{\text{red}} = 0.0016$), and -50°C ($P_{\text{red}} = 0.0008$) using plain and microporous-coated copper samples. The effects of saturation temperature and microporous coatings on the HTC and CHF are reported. The test results combined with experimental data taken from the literature are then used to develop HTC and CHF correlations that are applicable for low-temperature saturated conditions. Heat transfer results from this study were used to design two-phase-based cooling systems for automotive hydrogen fueling applications (the hydrogen-related results are not reported in this paper). Refrigerant R-245fa was used for this study because it is a non-flammable refrigerant that is commonly used in passive two-phase cooling applications.

2 Materials and Methods

2.1 Boiling System Description

A schematic of the pool boiling system that was used to conduct the experiments is shown in Figure 1. The main system components are the pool boiling vessel, test sample, low-temperature chiller, power supply, and the computer/data acquisition system. The aluminum pool boiling vessel is cylindrical in shape and has an inner diameter of 88.9 mm, an outer diameter of 140 mm, and an axial length of 203 mm. Finite element structural analysis was conducted to design the pool boiling vessel and to ensure its structural integrity at the operating temperatures and pressures. An 89.3-mm-diameter pressure-rated borosilicate glass viewport is axially centered on one side of the vessel to allow for boiling visualization of the test sample. The vessel was supported using two 9.5-mm-diameter stainless-steel threaded rods inserted into the lower side of the vessel and an aluminum stand. The relatively thin threaded rods minimized contact between the vessel and the aluminum stand to reduce heat conduction to the vessel. During experiments, the boiling vessel and chiller tubing were insulated with thick layers of flexible foam insulation to minimize heat gain from the laboratory environment.

Figure 2 shows the computer-aided design drawing of the horizontally oriented test sample fixture. The copper (oxygen-free copper) cylinder was the heated component and simulated a hydrogen-filled tube. The cylinder had a total length of 28.4 mm and an outer diameter of 14.3 mm. Two-millimeter-long extensions on either side of the copper cylinder supported the O-rings that provided the fluid seal. The cylindrical sample's boiling surface (i.e., the surface in contact with the fluid) had a diameter of 14.3 mm and a length of 24.5 mm. A 14.3-mm-diameter (9/16 inch) sample size was used because it represents the largest tube diameter size that is rated for the high pressures (≈ 100 MPa) that are typical for hydrogen-refueling applications. A cartridge heater was inserted within the copper cylinder to generate heat. The 6.35-mm-diameter cartridge heater had a total heated length of 25.4 mm and was centered within the copper cylinder. Thermal grease was applied at the heater-copper cylinder interface to minimize the thermal contact resistance.

The heater size can affect the boiling performance. Boiling on smaller heaters can be dominated by surface tension forces and thus their performance may deviate from the "classic" boiling curve behavior [19]. Buoyancy-dominated boiling heat transfer is typical for larger heated surfaces and normal gravity conditions. The ratio of the characteristic heater length to the capillary length ($L_b = \sqrt{\sigma/g(\rho_l - \rho_v)}$) has been used to determine if boiling on a heated surface will be dominated by surface tension or buoyancy forces. Bakhru and Lienhard [20] studied the heater size effect using small-radius (r) wires with various fluids. Their results show that boiling is dominated by buoyancy effects when $r/L_b > 0.15$. Raj and Kim [21] evaluated the effect of heater size on pool boiling using square heaters. They report that boiling is dominated by buoyancy effects when the length (one side length) of the heater is $> 2.1 \times L_b$. In this study, the largest L_b value is 1.3 mm (at $T_{sat} = -50^\circ\text{C}$), which results in $r/L_b = 5.7$. This indicates that the heater used for this study is representative of a larger heater and its boiling performance should be consistent with the behavior of the "classic" pool boiling curve.

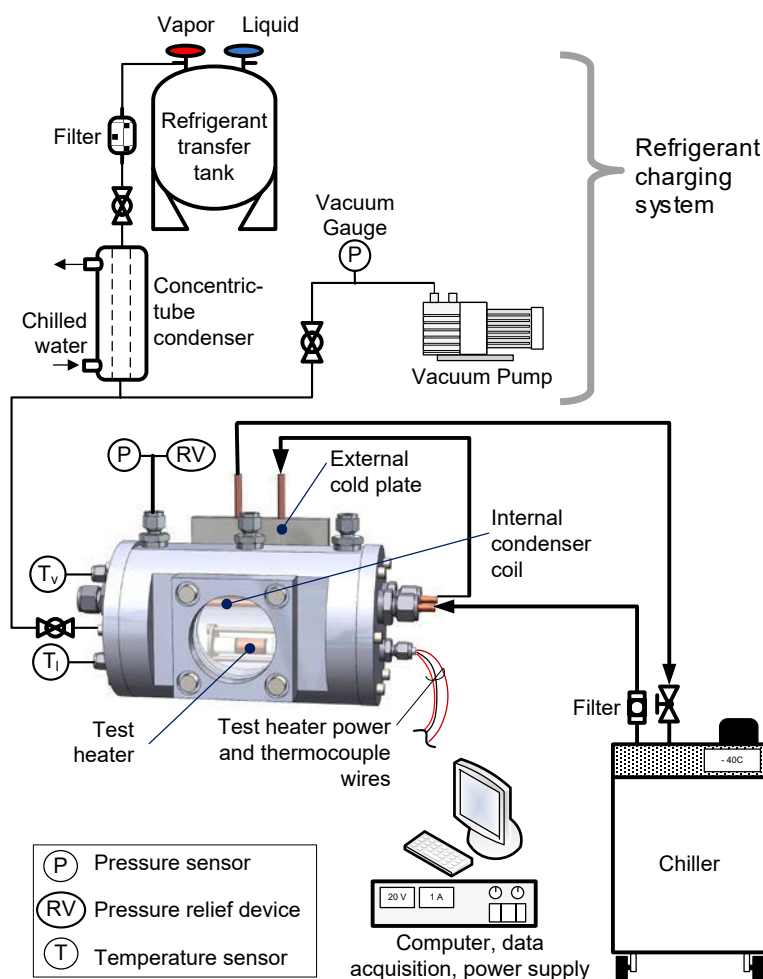


Figure 1. Schematic of the low-temperature boiling apparatus.

Stainless-steel flanges and bolts were used to secure the copper cylinder between two polyether ether ketone (PEEK) custom-fabricated fittings. Three 36 American wire gauge K-type thermocouples were inserted (with thermal grease) into 0.8-mm-diameter holes drilled at 90° intervals to measure the top, bottom, and side sample temperatures. The test sample was housed within the lower half of the boiling vessel and secured to one of the aluminum flanges via a 6.35-mm-diameter stainless steel tube and fittings. The test sample thermocouple wires and cartridge heater leads were routed through one of the PEEK fittings and stainless-steel tubing to the exterior of the vessel.

An FTS Systems RC210 Ultra-Low-Temperature Recirculating Chiller was used to control the refrigerant saturation temperature. The chiller circulated Golden HT80 coolant through a condenser coil located within the boiling vessel and an external cold plate attached to the back side of the vessel to maintain saturation temperatures as low as -50°C (Figure 1). A total of 1,050 W of heat can be rejected by the chiller at -40°C coolant temperature. For reference, the maximum heat generated by the test samples during the boiling tests was approximately 300 W.

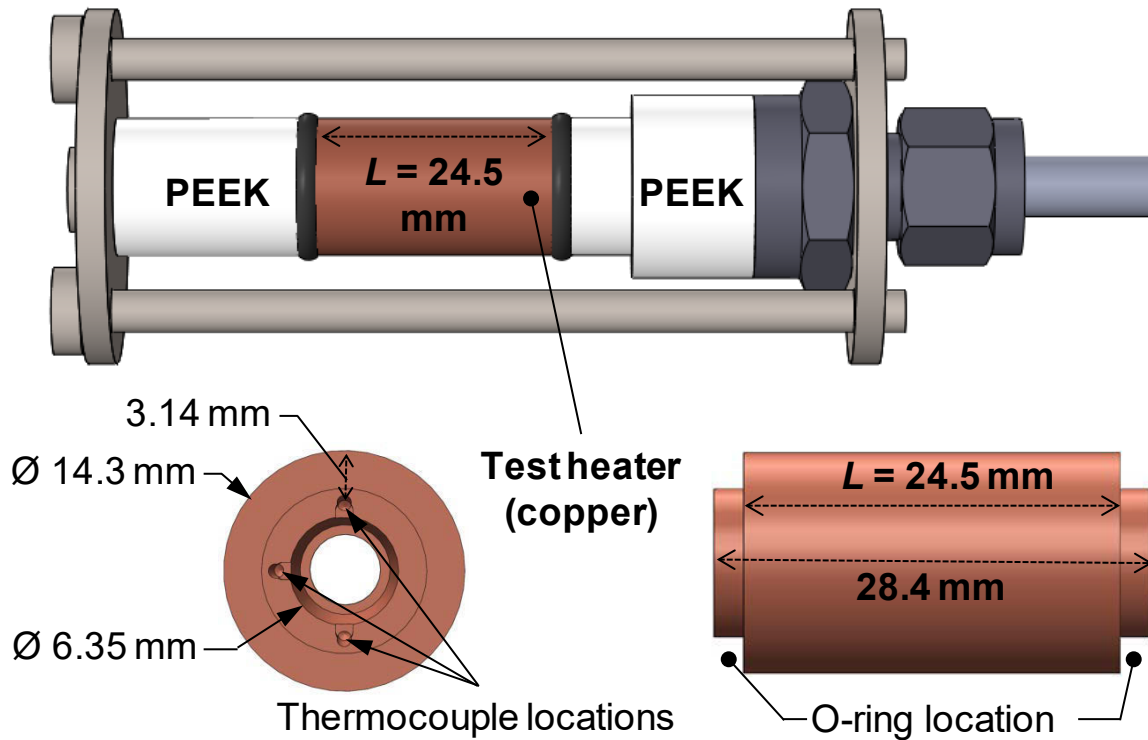
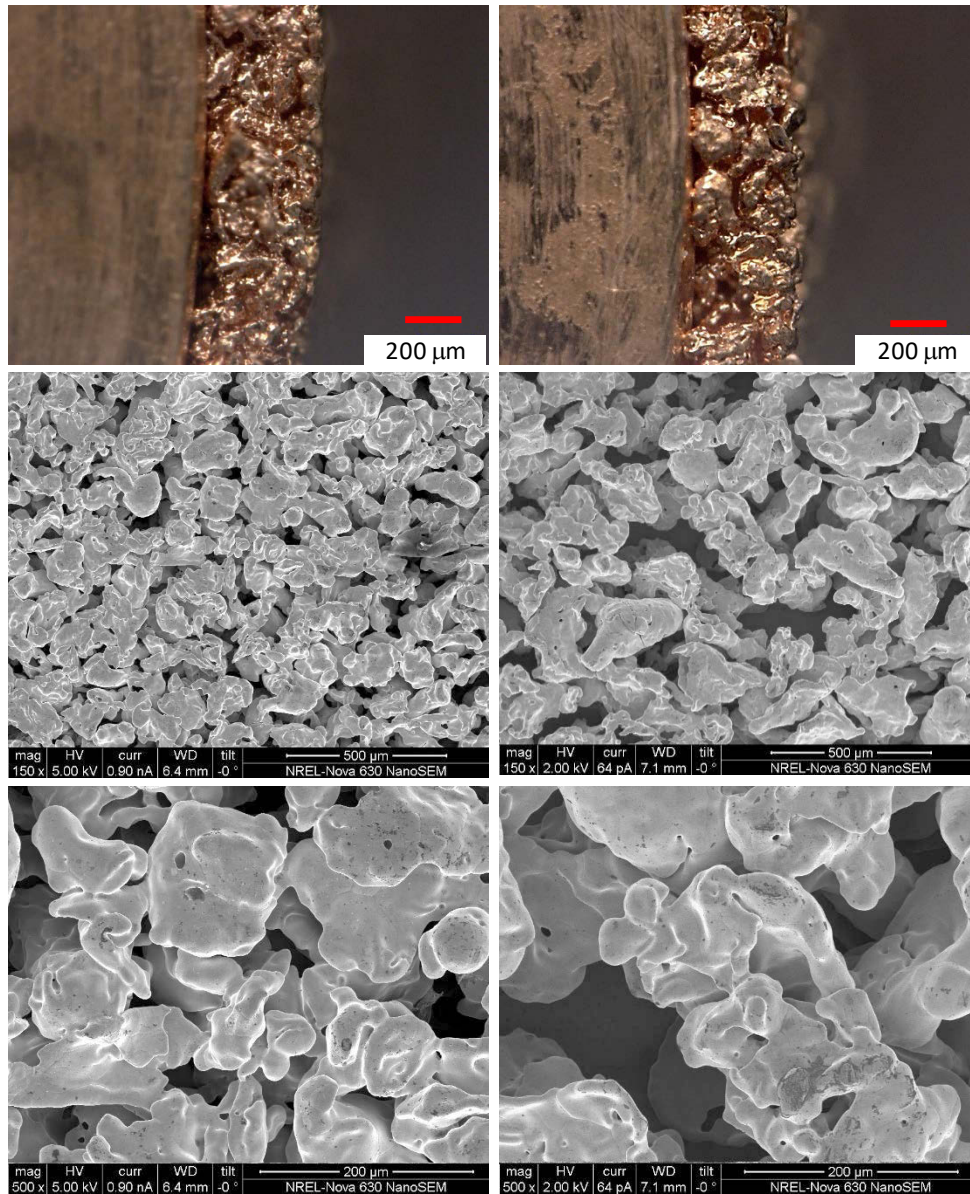


Figure 2. Computer-aided drawings of the cylindrical test sample and detailed views of the copper cylindrical test sample.

2.2 Microporous Coating Description

Two microporous-coated samples were tested to quantify their effect on boiling heat transfer. The coatings were bonded to the 14.3-mm-diameter surface of the copper samples by Celsia Inc. using a sintering process. Copper powder containing particles of varying irregular shapes (i.e., not spherical) were used to fabricate the coatings. For one sample (Microporous 1), the powder was sifted through a mesh (mesh number 120) to obtain particles less than $125\ \mu\text{m}$ in size that were then sintered to the sample. For the second sample (Microporous 2), the powder was processed through two mesh sizes (mesh numbers 60 and 120) to collect particles with sizes between $125\ \mu\text{m}$ and $250\ \mu\text{m}$ that were then sintered to the sample. Sintering the particles created the microporous structure shown by the digital microscope and scanning electron microscope (SEM) images provided in Figure 3. The coating thickness for both microporous samples were measured to be approximately $450 \pm 50\ \mu\text{m}$. Digital microscope and SEM measurements indicated that the Microporous 2 sample contains larger cavities as compared with Microporous 1 (Figure 3). Sample weight and volume measurements were used to estimate the porosity of the two coated samples. The porosity for Sample 1 and Sample 2 were computed to be approximately 65% and 68%, respectively.

The performances of the two microporous samples were compared to each other to evaluate the effect of particle size on thermal performance, and also compared to the performance of the plain/non-coated copper sample. The surface roughness of the plain copper sample was measured at various locations using a laser profilometer. The average surface roughness of the plain sample was measured to be $R_a = 1.1\ \mu\text{m}$.



Microporous 1

Microporous 2

Figure 3. Digital microscope images showing a side view of the coating (top two images) and SEM images of the Microporous 1 (left) and Microporous 2 (right) samples.

2.3 Procedures

First, the boiling vessel and test samples were disassembled, rinsed, and wiped down using isopropanol alcohol to remove contaminants left behind from the machining process. The test sample fixture (Figure 2) was then assembled and attached to the vessel's end flange. The flange with test sample assembly was then bolted to the boiling vessel to position the test sample within the lower half of the vessel.

A vacuum pump, oil-free pneumatic compressor, refrigerant transfer tank, water-cooled condenser, and charcoal filter were used to transfer refrigerant to and from the vessel. The pneumatic compressor was only used during the refrigerant recovery process and not used during filling. The vacuum pump was used to remove air from the vessel prior to charging. The vessel was considered to be air-free and ready for charging when the interior vessel pressure dropped below 10 Pa. The vacuum pump was then isolated by closing a ball valve.

R-245fa was transferred to the vessel using a distillation process. The process involved connecting the boiling vessel to the vapor side of the refrigerant transfer tank and using a heat exchanger, located above the vessel, to condense the vapor (Figure 1). The distillation process continued until the liquid refrigerant reached a level of about 25 mm above the test sample's upper surface. At that point, the valves connecting the transfer tank to the vessel were closed, and the transfer tank and vacuum pump were disconnected from the vessel. The distillation process combined with the charcoal filter (located between the transfer tank and vessel) provided clean refrigerant to the vessel. After charging, pressure versus temperature measurements were taken and compared to R-245fa saturated data from the National Institute of Standards and Technology (NIST) [22] to verify saturated conditions.

The chiller was then turned on, and its set-point temperature was adjusted to achieve refrigerant saturation temperatures of -30°C, -40°C, or -50°C. Once the target saturation temperature was reached, pressure and temperature measurements were again taken and compared against R-245fa saturated data from NIST [22]. Pool boiling experiments were initiated after saturated conditions were confirmed. During the pool boiling experiments, the chiller set-point was adjusted as the sample heat was increased (e.g., the set-point was lowered for the increasing heat flux conditions) to maintain constant pressure conditions.

Experiments were controlled and monitored using a LabVIEW-based program. The program controlled a National Instruments CompactDAQ data acquisition system and an adjustable Agilent N5771A power supply to generate heat-flux-controlled boiling curves. The power supply powered the cartridge heater located within the test sample. The heat flux was increased in 5 kW/m² increments in the low heat flux, single-phase regime and increased in 10 kW/m² increments at higher heat fluxes near the CHF. The onset of CHF was identified by a sudden temperature increase ($\Delta T > 50$ K) for all three sample thermocouples. The power to the cartridge heater was automatically turned off by the program when the CHF condition was detected. CHF was defined as the average between the heat flux at which CHF occurred and the heat flux value just before the CHF condition. Every test condition was repeated three times to evaluate the repeatability of the data.

Sample wall superheat temperatures (T_w) were calculated using the three thermocouples inserted within the sample and assuming one-dimensional and steady-state heat transfer (Equation 1).

$$T_w = \bar{T} - \frac{q \ln(r_2/r_1)}{2\pi Lk} \quad \text{Equation 1}$$

where \bar{T} is average temperature of the three sample thermocouples, q is the total heat dissipated by the cartridge heater, r_2 is external surface radius, r_1 is the thermocouple location radius, and L is the heated

sample length. The use of the averaged thermocouple temperatures \bar{T} to compute T_w is consistent with prior studies by Webb and Pais [12]. The copper thermal conductivity (k) value of 401 W/m-K (for -20°C [23]) was used to account for the low-temperature conditions. The uncertainty of the k value on the T_w and HTC calculations was evaluated in Section 2.4 (Uncertainty Analysis).

The HTCs (h) were computed using Equation 2.

$$h = \frac{q}{D\pi L(T_w - T_l)} \quad \text{Equation 2}$$

where D is the sample's outer diameter and T_l is the liquid temperature. The refrigerant liquid (T_l) and vapor (T_v) temperatures were measured using two K-type probe thermocouples inserted in the lower (liquid side) and upper (vapor side) sections of the vessel (see Figure 1). This diameter (D) is the un-coated surface diameter and was used for both the plain and microporous samples.

2.4 Uncertainty Analysis

Finite element (FE) analysis was used to design the test sample and to estimate the heat loss through the sample support structure (i.e., PEEK supports, O-rings, tubing). A detailed computer-aided design model of the test sample was developed and used in the FE simulations. The model included all the test sample components including the copper cylinder, cartridge heater, PEEK fittings, O-rings, stainless-steel compression fixture, thermal grease (between heater and cylinder), stainless-steel support tube, and electrical wires. Measured HTCs for the plain surface were imposed as boundary conditions on the external test sample surface to model boiling heat transfer. The FE-computed heat losses through the support structure (i.e., non-boiling surface) were estimated to be approximately 2% at a heat flux of 100 kW/m² (Figure 4). The thermal losses for the microporous-coated sample will be lower than those of the plain sample due to microporous-coating's higher HTCs. The heat flux values reported were not adjusted to account for the estimated heat loss due to the small magnitude of the thermal losses.

An uncertainty analysis was conducted following the procedures outlined by Dieck [24] to quantify the uncertainty of the measured values. The K-type thermocouples, pressure transducer, and digital voltmeters were calibrated using NIST traceable practices and equipment. The systematic and random uncertainty values for the measurements were gathered and used in the propagation-of-error equation to estimate the uncertainty of the computed values. The uncertainties were computed at a low (20 kW/m²) and a high heat flux value (250 kW/m²) to quantify the uncertainty within the experimental heat flux range. The analysis indicates that at 20 kW/m², the uncertainties in the wall superheat, heat flux, and HTC values were ± 0.5 K, $\pm 3\%$, and $\pm 12\%$, respectively. At 250 kW/m², the uncertainties in the wall superheat, heat flux, and HTC values were ± 0.4 K, $\pm 1\%$, and $\pm 3\%$, respectively. A ± 5 W/m-K copper thermal conductivity (k) uncertainty was assumed for these calculations to account for the temperature variation of the copper sample and its effect on k . The vapor pressure was measured using a Setra 280E absolute pressure transducer (0–172 kPa range) with an uncertainty of ± 1.2 kPa. The uncertainty in a calibrated thermocouple measurement (e.g., liquid and vapor temperatures) was conservatively estimated at ± 0.1 K. All stated uncertainties were computed at a 95% confidence level.

The estimated uncertainty values are represented by error bars in the figure plots. In some cases, the uncertainty values are small and thus are hidden behind the data symbols—this is the case for the heat flux uncertainty values which are relatively small.

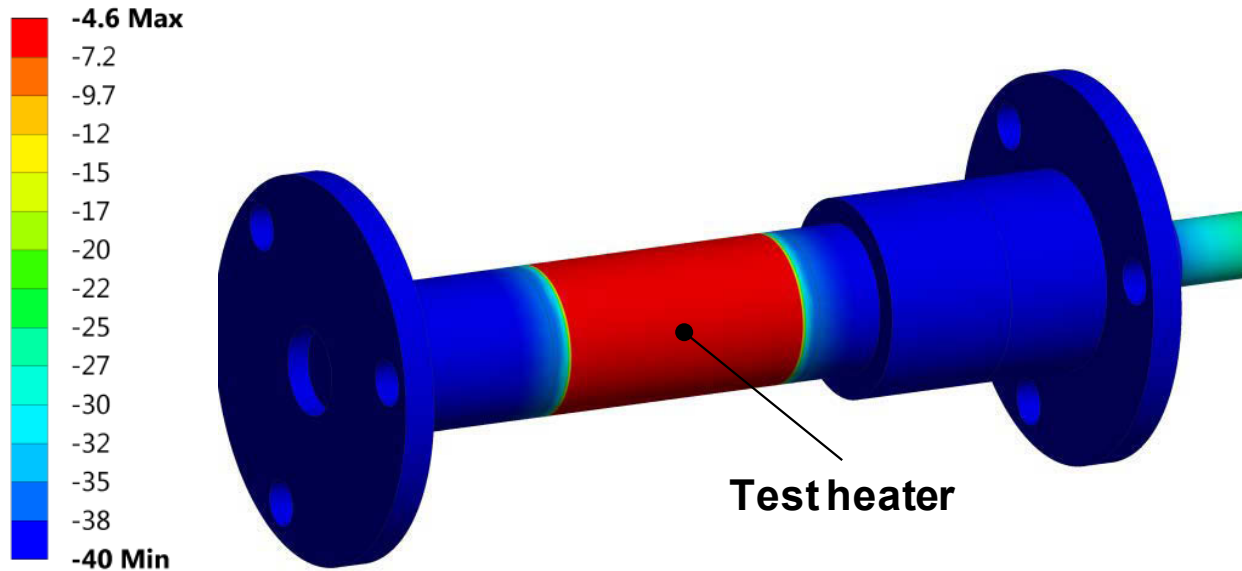


Figure 4. FE-generated temperature contours of the test sample used to estimate the heat loss through the insulation and to design the test sample. Legend values are in degrees Centigrade.

3 Results and Discussion

Experiments were conducted to measure the pool boiling performance of saturated R-245fa at low temperatures ($T_{\text{sat}} = -30^{\circ}\text{C}$, -40°C , and -50°C). The low saturation temperatures are relevant for hydrogen precooling in select fuel-cell vehicle fueling applications. Relevant R-245fa saturated properties are provided in Table 1. In this section, the pool boiling results for the plain test sample are presented and compared with available HTC and CHF correlations. Then the thermal performance for the two microporous-coated samples are reported and compared with the plain sample. The experimental results are then used to develop HTC and CHF correlations applicable for low-temperature conditions.

| T_{sat} | P | P_{red} | ρ_l | μ_l | ρ_v | k_l | $h_{l,v}$ | σ |
|--------------------|--------------|------------------|------------------------|---------------|------------------------|------------------------|-----------------------|---------------------|
| $^{\circ}\text{C}$ | MPa | | kg/m^3 | Pa s | kg/m^3 | $\text{kW}/\text{m K}$ | kJ/kg | N/m |
| -50 | 0.003 | 0.0008 | 1523.5 | 0.0015 | 0.21 | 1.15×10^{-4} | 230.7 | 0.023 |
| -40 | 0.006 | 0.0016 | 1500.5 | 0.0012 | 0.40 | 1.12×10^{-4} | 225.7 | 0.022 |
| -30 | 0.011 | 0.0030 | 1477.1 | 0.0009 | 0.74 | 1.08×10^{-4} | 220.7 | 0.021 |

Molecular mass = 134 g/mol

Table 1. R-245fa saturated properties at $T_{\text{sat}} = -30^{\circ}\text{C}$, -40°C , and -50°C from NIST [22].

3.1 Plain (non-coated) Sample Results

Figure 5 plots the boiling HTCs versus the heat flux for the plain sample at $T_{\text{sat}} = -30^{\circ}\text{C}$ ($P_{\text{red}} = 0.003$), -40°C ($P_{\text{red}} = 0.0016$), and -50°C ($P_{\text{red}} = 0.0008$) (single-phase portions are not included). As expected, the HTCs are found to increase with increasing saturation temperature. Measured HTCs were relatively low ($<4 \text{ kW}/\text{m}^2\text{-K}$) for two-phase cooling standards. The low HTCs are associated with the low reduced pressures at which these tests were conducted. Decreasing P_{red} values are well known to decrease HTCs [2–5,12].

Surface tension increases as the saturation pressure and temperature decrease, resulting in larger departure bubble diameters. This is the case for the current study where relatively large bubble diameters (on the order of several millimeters) were observed to originate from plain sample at $T_{\text{sat}} = -50^{\circ}\text{C}$ (Figure 6). The bubble departure frequency is typically considered to be inversely proportional to the bubble departure diameter [19] and thus the bubble residence time should increase at lower saturation temperatures. The combined effects of larger bubble sizes and lower departure frequencies means that more of the heated surface will be covered in vapor at lower pressures (as compared with higher pressures). The increase in surface vapor coverage combined with a decrease in the number of active nucleation sites will in turn negatively affect both the HTCs and CHF values. The effect of pressure and temperature on active nucleation sites is discussed in Section 3.2, Microporous-Coated Sample Results.

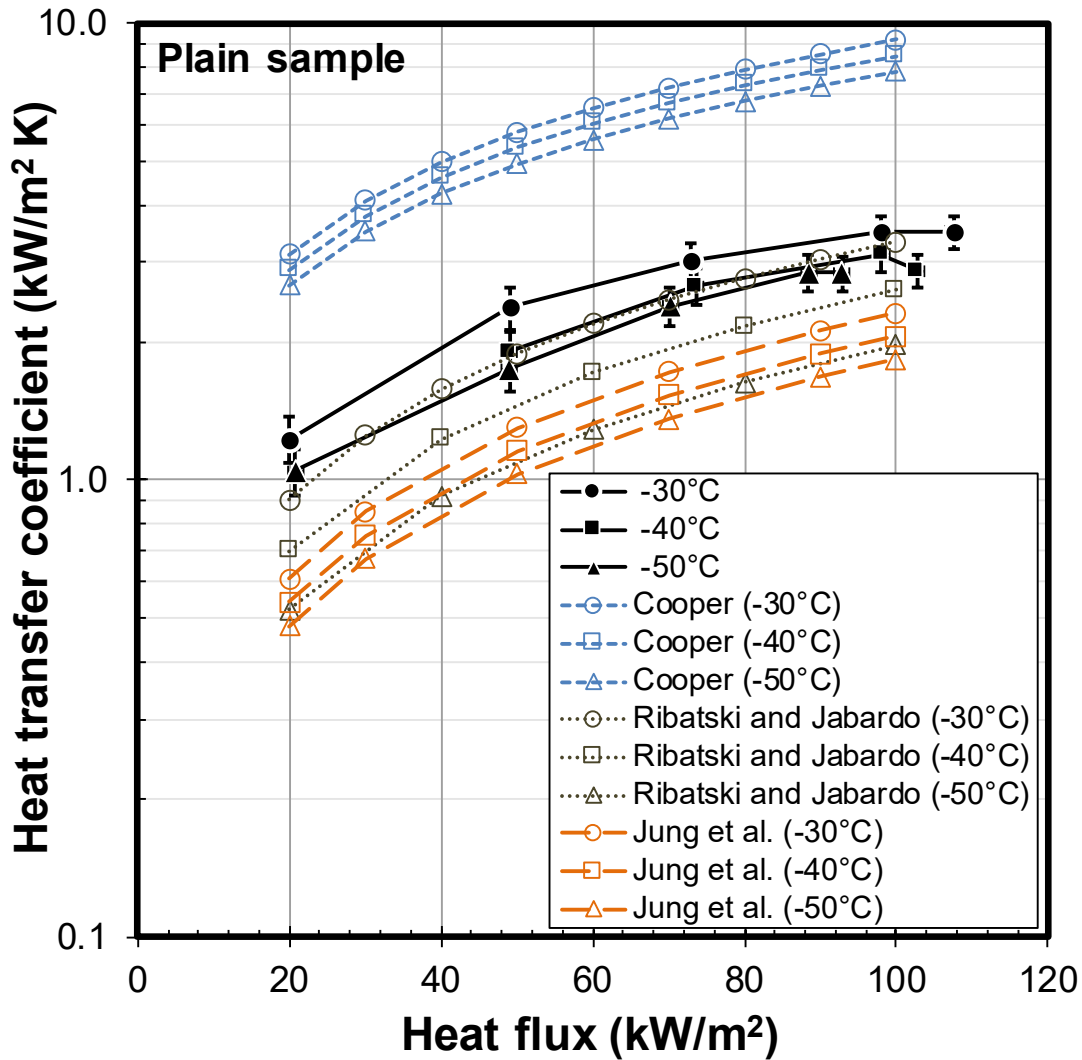


Figure 5. Boiling HTCs versus heat flux for the plain sample. Also plotted are the predicted HTCs from various correlations. Reference data sources: Cooper [25], Ribatski and Jabardo [11], and Jung et al. [26].

The measured HTCs were compared with the HTC correlations from Cooper [25], Ribatski and Jabardo [11], and Jung et al. [26] (Figure 5). The correlation equations are provided in Table 2. For a given heat flux and saturation temperature, each correlation predicts a different HTC, and current results fall in between the HTCs predicted by the three correlations. As suggested by Gorenflo et al. [27] and Jones et al. [28], the relation $R_a \approx 0.4 \cdot R_p$ was used to compute R_p (Glattungstiefe, an outdated surface measurement metric) the surface roughness parameter used in the Cooper correlation. This relation predicts a relatively large R_p value ($R_p = 2.8 \mu\text{m}$). The large R_p and the uncertainty associated with its value combined with the low saturation temperature (i.e., low P_{red}) are believed to be the reason for the large discrepancy between the Cooper correlation and current experiments. The experimental results were best predicted with the Ribatski and Jabardo [11] correlation. This correlation yielded a maximum error of about 48% at $T_{sat} = -50^\circ\text{C}$. The Jung et al. [26] correlation predicts the lowest HTC values and underpredicts the results of this study. The lowest P_{red} values used to develop the Ribatski and Jabardo [11] and Jung et al. [26] correlations were 0.008 and 0.04, respectively. Although both cases used P_{red} values higher than those of

the current study, the Ribatski and Jabardo [11] P_{red} values are lower, and thus closer to the P_{red} values of this study. This is believed to be the reason the Ribatski and Jabardo [11] correlation provides a better match to the current results.

The sample was designed in such a way that the O-ring extended beyond the diameter of the samples and completely covered the side surfaces (axial-end faces) of the samples. This was an attempt to prevent liquid from contacting the sides of the samples and to minimize edge boiling effects. However, in some cases (not all) boiling was observed to begin at the O-ring-sample interface. These edge-boiling effects will affect the boiling incipient superheat and HTC's in the lower heat flux boiling regime. However, the effect of any edge boiling should diminish in the fully developed boiling regime due to the small surface area of the edges as compared to the boiling surface area (14.3 mm diameter and 24.5 mm long).

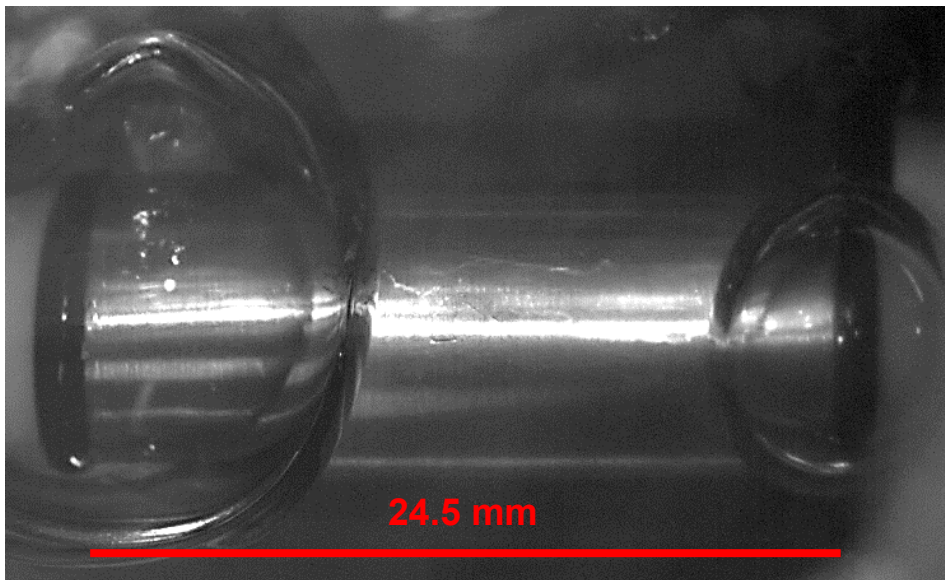


Figure 6. High-speed video image of the plain sample showing the relatively large bubble sizes generated at a low saturation temperature of -50°C (heat flux = 20 kW/m^2).

The plain sample CHF values versus the saturation temperature are provided in Figure 7. Plain surface CHF values were relatively low ($<120\text{ kW/m}^2$) and were found to decrease with decreasing saturation temperature. This trend is to be expected for the low reduced-pressure conditions ($P_{red} < \approx 0.3$) [3–5] used in this study. The CHF results were then compared with two CHF correlations for cylindrical geometries from Lienhard and Dhir [29] and Sun and Lienhard [30] (Table 3). Both correlations are based on the Helmholtz instability CHF mechanism and are variations of the well-known Zuber correlation [31]. As shown in Figure 7, the two CHF correlations predict similar CHF values and deviate by as much as about 48% from the measured values. Discrepancies between the correlations and the current data may be associated with fluid wettability and surface roughness effects that are not considered in the models. The experimental results were then used to develop a CHF correlation applicable for low-saturation-temperature conditions. The proposed CHF correlation is discussed in Section 3.3, Correlating the Results.

| | |
|---------------------------|--|
| Cooper [25] | $h = 95 q^{0.67} P_{red}^{(0.12-0.2 \log_{10} R_p)} (-\log_{10} P_{red})^{-0.55} M^{-0.5}$ |
| Ribatski and Jabardo [11] | $h = 100 P_{red}^{0.45} (-\log_{10} P_{red})^{-0.8} R_a^{0.2} M^{-0.5} \frac{q^{(0.9-0.3 P_r^{0.2})}}{A}$ |
| Jung et al. [26] | $h = 41.4 \frac{k_l}{D_b} \left[\frac{(q'') D_b}{k_l T_{sat}} \right]^{[0.835(1-P_{red})]^{1.33}} (-\log_{10} P_{red})^{-1.52} \left(1 - \frac{\rho_v}{\rho_l} \right)^{0.53}$ |

Table 2. HTC correlations taken from the literature.

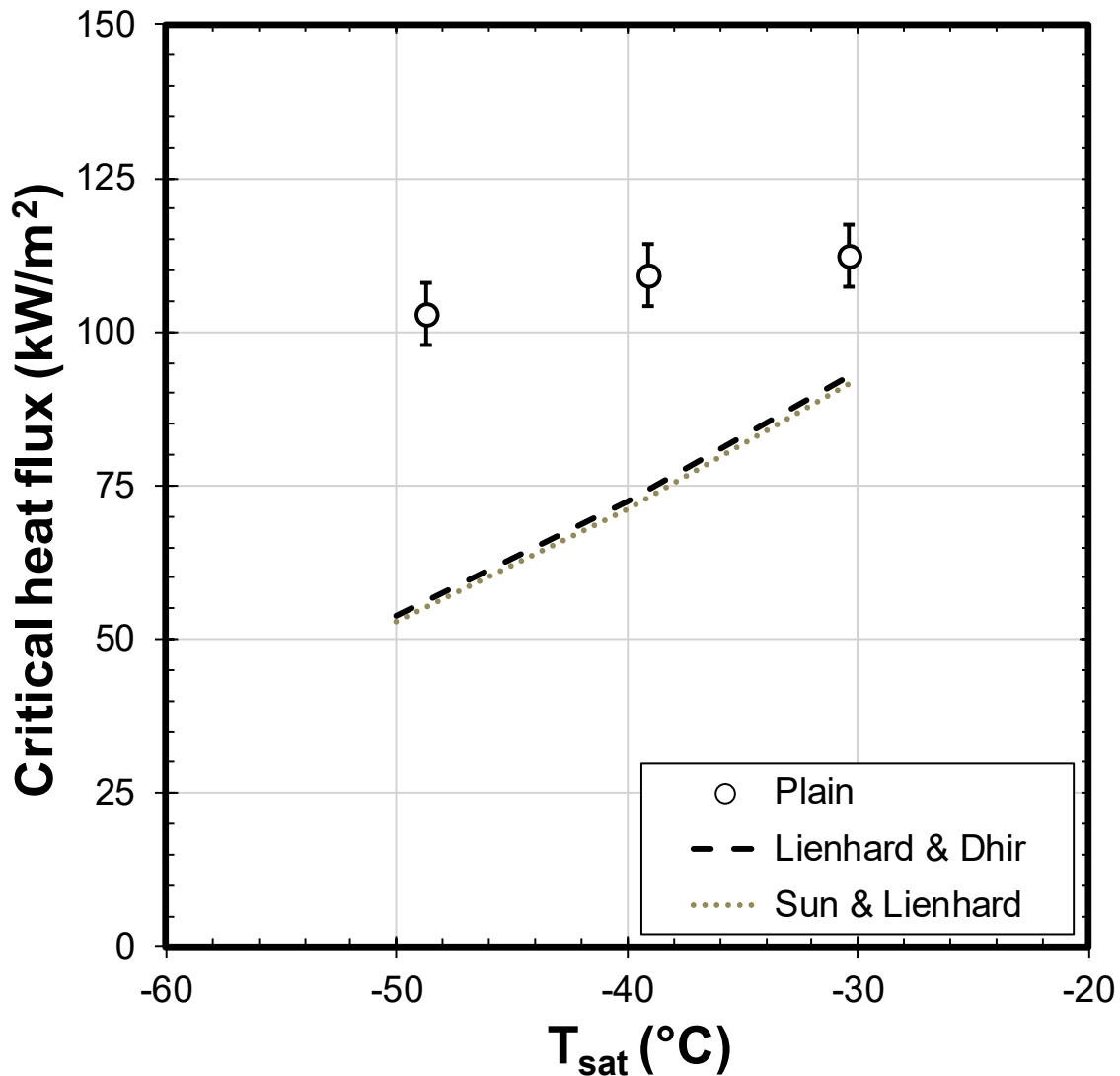


Figure 7. CHF versus saturated temperature for the plain sample. Reference data sources: Lienhard and Dhir [29] and Sun and Lienhard [30].

| | |
|------------------------|--|
| Lienhard and Dhir [29] | $q''_{CHF} = 0.904 q''_{CHF,Z}$ |
| Sun and Lienhard [30] | $q''_{CHF} = 0.89 + 2.27e^{(-3.44\sqrt{R'})} q''_{CHF,Z}, r' = r \sqrt{\frac{g(\rho_l - \rho_v)}{\sigma}}$ |

Table 3. CHF correlations taken from the literature.

3.2 Microporous-Coated Sample Results

The boiling curves for the Microporous 1 and plain samples are provided in Figure 8. The Microporous 1 coating was found to increase boiling HTC from approximately 330% to 460% as compared with the baseline, plain sample. Additionally, this coating increased the CHF by approximately 140%. The boiling curves for the Microporous 2 and plain samples are shown in Figure 9. Tests with the Microporous 2 sample were only conducted at $T_{sat} = -30^\circ\text{C}$ and -40°C . A visual comparison between Figures 8 and 9 reveals that the two microporous coatings have similar boiling heat transfer performance. Figure 10 compares the HTCs for both microporous coated samples at the different saturation temperatures. As shown, HTCs for both coatings are similar—within uncertainty estimates. Similarly, the CHF enhancements from the Microporous 2 sample were nearly identical to the CHF enhancements provided by the Microporous 1 sample (about 140%). Changing the saturation temperature had minimal effect on the magnitude of the HTC and CHF enhancements provided by both coatings. Although Microporous 2 was not tested at the lowest temperature, based on the available data it is reasonable to assume that the performance for Microporous 2 at $T_{sat} = -50^\circ\text{C}$ would be similar to the performance of Microporous 1 at $T_{sat} = -50^\circ\text{C}$.

Pool boiling tests using decreasing heat-flux conditions were also conducted. The results for $T_{sat} = -40^\circ\text{C}$ are shown in Figures 8 and 9. The hysteresis effects associated with the elevated superheat at boiling incipience for the increasing heat flux condition are evident when comparing the boiling curves generated using increasing and decreasing heat fluxes.

The HTCs for the microporous samples achieve a maximum value at about 200 kW/m^2 , then decrease with increasing heat flux. This HTC trend is consistent with what others have reported for microporous samples and is believed to be associated with the formation of a thin vapor layer within the coating at higher heat fluxes [32,33]. After the vapor layer appears, its size grows as the heat flux is increased, resulting in a further decrease of the HTC and eventually leading to CHF. The use of thinner coatings [32] or hierarchical microporous structures [33] have been shown to be effective techniques to reduce the formation of the vapor layer and improve boiling performance.

The coatings' HTC enhancements are in part due to an increase number of active nucleation sites from a wide range of cavity sizes provided by the coatings. Figure 11 shows two high-speed video images taken at a 10-millisecond interval and at a heat flux of 100 kW/m^2 for the plain and the two microporous-coated samples. Relatively larger non-boiling patches are seen for the plain sample (Figure 11, top). The two microporous-coated samples show a more even distribution of nucleation sites on the heated surface. Additionally, the coatings also enhance HTC and CHF via increased surface area, increased evaporation due to an increase in the three-phase contact line from the numerous tunnels within the coating and

passive fluid transport within the coating via capillary wicking effects. The coatings were proven to be an effective means to increase the relatively low HTC and CHF of the plain surface at very low temperatures.

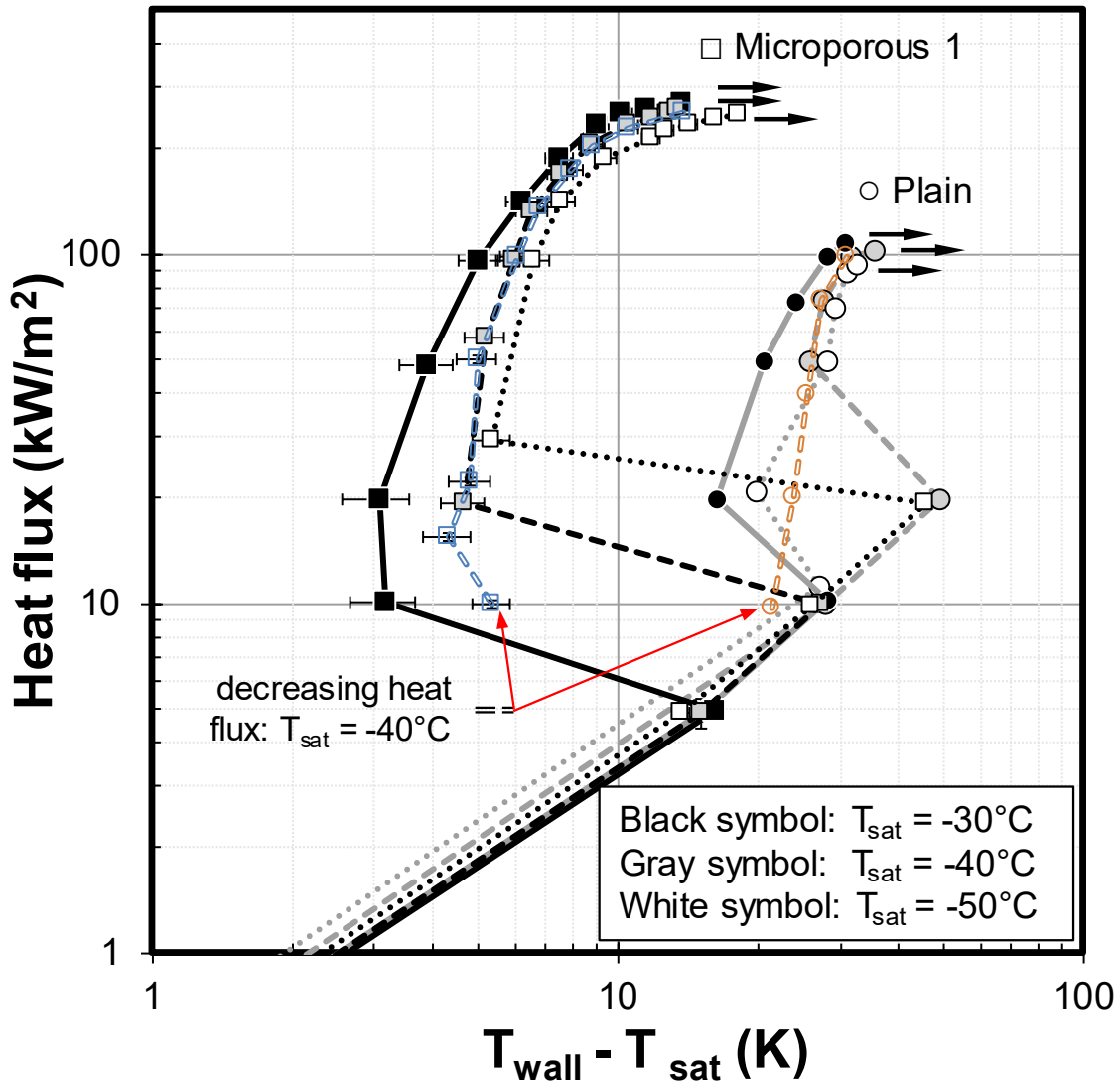


Figure 8. Boiling curves for the Microporous 1 and plain samples. The arrows denote the onset of CHF.

Surprisingly, the wall superheat required to initiate boiling was relatively high for the two microporous samples. The boiling incipient superheat values for the plain coating ranged from 21 K to 60 K while the boiling incipient superheat values for the microporous samples ranged from 3 K to 46 K. On average, the boiling incipient superheat for the microporous-coated samples were lower than those of the plain sample. However, in some cases, the incipient superheat values for the plain sample were lower than those of the microporous-coated surface. This behavior differs from what is typically observed at higher temperatures. For example, similar microporous coatings tested at saturation temperatures above 40°C using R-245fa, R-134a, and R1234yf required less than 5 K of superheat to initiate boiling [4,5]. The

relatively high boiling incipient superheat and lower HTC's are likely associated with a decrease in the number of active nucleation sites at low saturation temperatures. A better understanding of the effect of fluid temperature on the number of active nucleation sites can be gained by analyzing how nucleation is believed to occur on solid surfaces for highly wetting fluids.

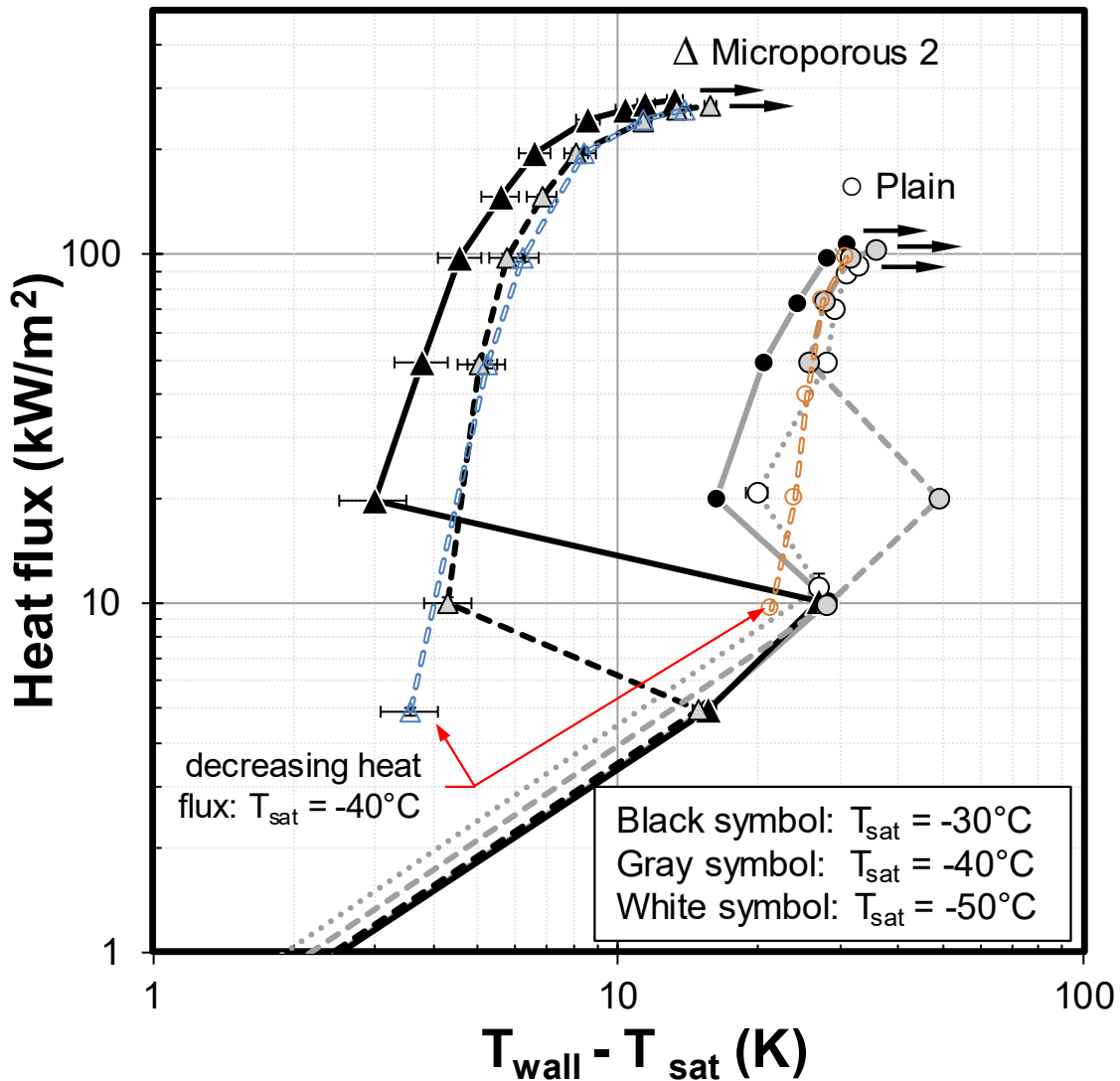


Figure 9. Boiling curves for the Microporous 2 and plain samples. The arrows denote the onset of CHF.

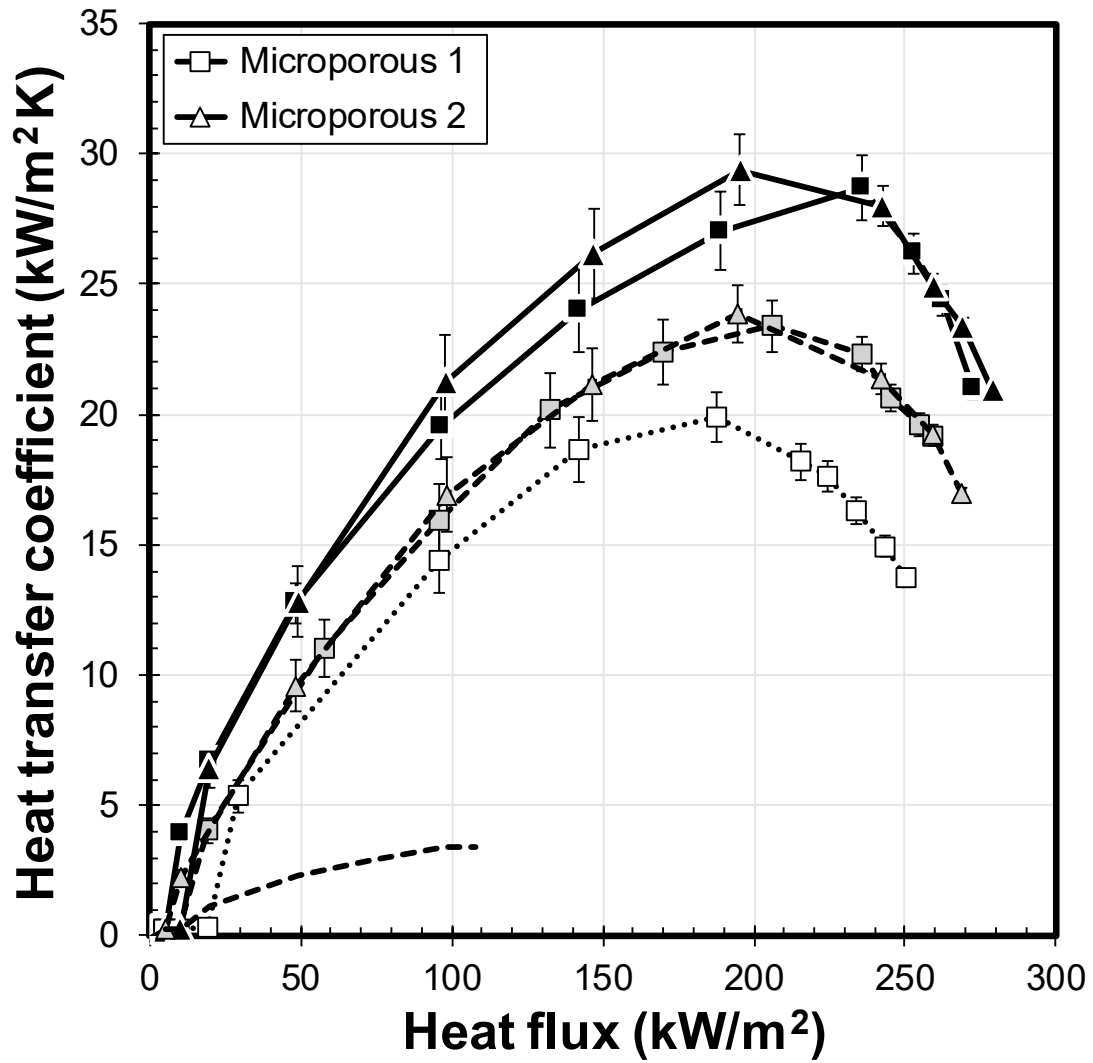


Figure 10. HTC versus heat flux for the two microporous-coated samples. Plain surface results are provided for reference.

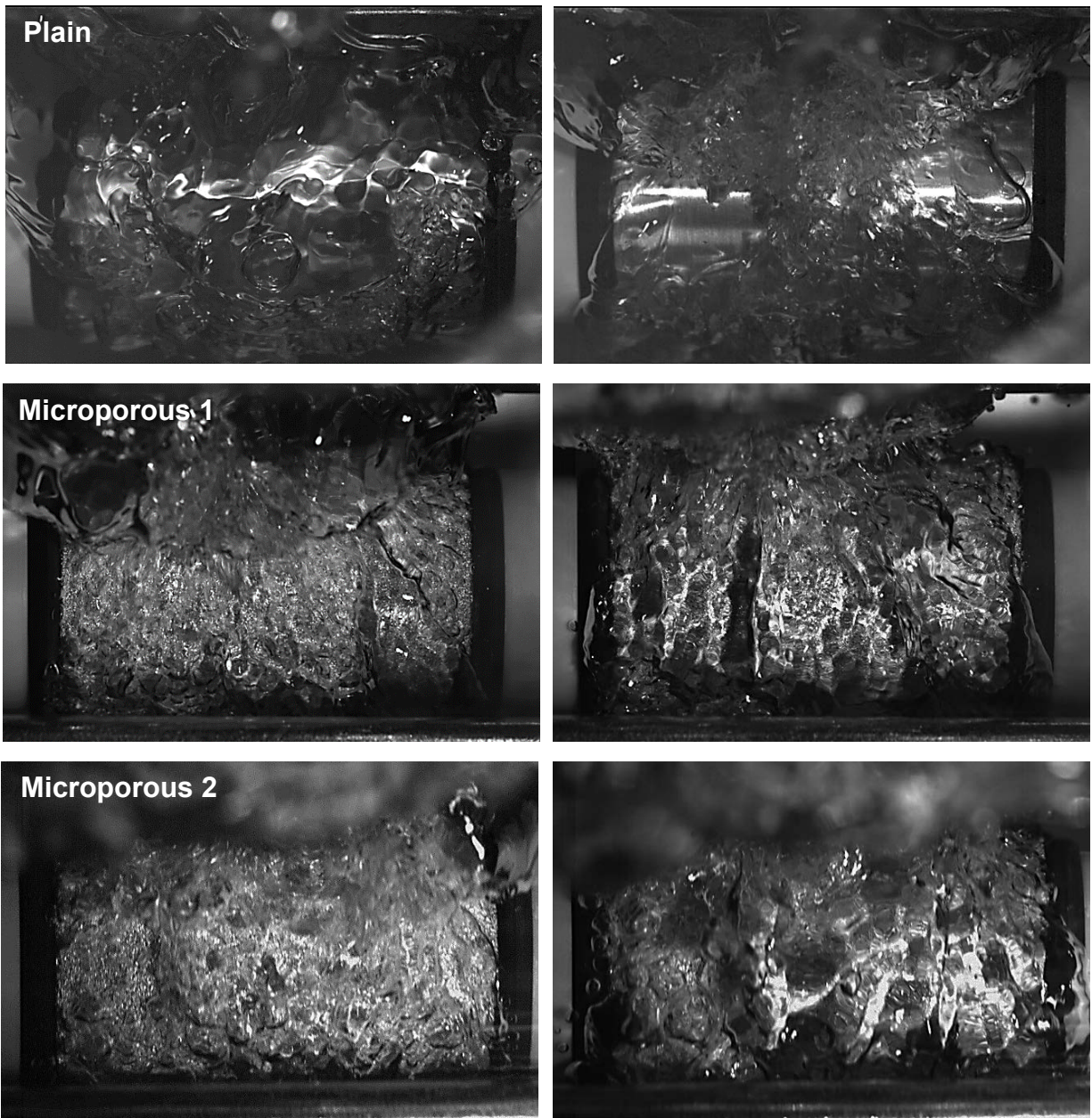


Figure 11. High-speed video images of the Plain, Microporous 1, and Microporous 2 samples at $T_{sat} = -30^{\circ}\text{C}$ and a heat flux of 100 kW/m^2 . The images on the right were taken 10 ms after the images on the left were taken.

Heterogeneous nucleation occurs within cavities containing small embryonic vapor/air bubbles. For the embryonic bubble(s) to grow beyond the cavity and nucleate, the temperature of the superheated liquid layer surrounding the bubble must exceed the saturation temperature corresponding to the vapor pressure within the bubble. According to You et al. [34,35], the incipient bubble size for highly wetting fluids may be estimated using the Young-Laplace equation.

$$r_b = 2\sigma_w / [P_{sat}(T_w) - P_{sat}(T_{sat})] \quad \text{Equation 3}$$

where r_b is the bubble radius, σ_w is the surface tension corresponding to the wall temperature, $P_{sat}(T_w)$ is the saturation pressure corresponding to the wall temperature, and $P_{sat}(T_{sat})$ is the saturation pressure corresponding to the fluid saturation temperature. In this case, $P_{sat}(T_w)$ is an estimate of the vapor pressure within the bubble. For a bubble to grow and nucleate (i.e., increase r_b), the pressure differential (i.e., wall superheat) must exceed the equilibrium condition stated in Equation 3.

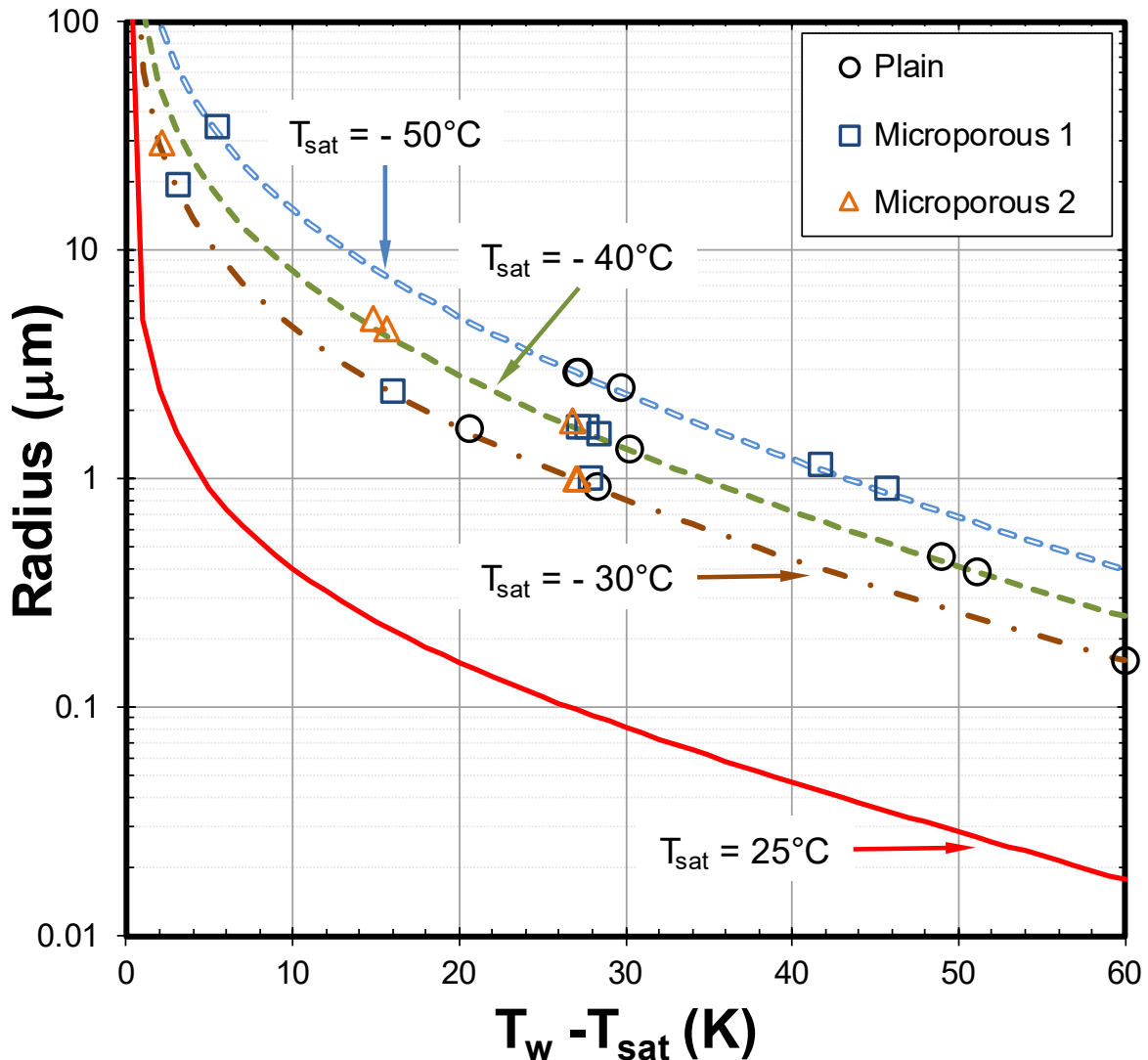


Figure 12. Incipient bubble radii versus wall superheat (per Equation 3) for R-245fa at $T_{sat} = 25^\circ\text{C}$, -30°C , -40°C , and -50°C . The experimentally measured boiling incipient superheat values for the plain and microporous-coated surfaces are provided.

Figure 12 plots the incipient bubble radius computed by Equation 3 versus the wall superheat for R-245fa at $T_{sat} = 25^\circ\text{C}$, -30°C , -40°C , and -50°C . The $T_{sat} = 25^\circ\text{C}$ case was provided for comparison with the lower temperatures. The boiling incipient superheat values for all tests conducted (includes the three test repetitions for every condition) and the corresponding incipient bubble sizes are also provided in Figure 12. This analysis suggests that it is harder (requires more superheat) to nucleate smaller bubbles at lower

saturation temperatures. For example, sustaining a 1- μm -radius bubble only requires about 5 K of superheat at $T_{sat} = 25^\circ\text{C}$ while more than 40 K of superheat is required at $T_{sat} = -50^\circ\text{C}$. This suggests that smaller surface cavities containing small embryonic bubbles are less likely to become active nucleation sites at lower temperatures. This effect is believed to decrease the number of active nucleation sites, which results in higher boiling incipient superheat values and lower HTC values at lower saturated temperatures/pressures.

The Microporous 2 sample was fabricated using larger particle sizes and thus the cavity/pore sizes within this coating are expected to be larger (compared to Microporous 1). This is supported by visual observations and measurements shown in Figure 3 that indicate that cavities in the Microporous 2 sample are larger. However, the results show that the performance of both coatings was similar—within uncertainty estimates. Therefore, it is believed that coatings with larger cavity sizes (larger than those used for the current samples) may yield better results for these low-temperature conditions.

3.3 Correlating the Results

The experimental results were then used to generate HTC and CHF correlations applicable for low-saturation-temperature conditions (down to $T_{sat} = -50^\circ\text{C}$). The modified version of the Cooper correlation [25] shown as Equation 4 was used to correlate the HTCs (h) for the plain sample. The Cooper equation was selected due to its simplicity relative to other correlations.

$$h = C_0 (q'')^{C_1} (-\log_{10} P_{red})^{C_2} P_{red}^{(0.12-0.2\log_{10} R_a)} M^{-0.5} \quad \text{Equation 4}$$

where q'' is the heat flux and M is the molecular weight. The least-squared linear regression method was used to compute the leading coefficient (C_0), the heat flux exponent coefficient (C_1), and the $-\log_{10} P_{red}$ exponent coefficient (C_2). Unlike the Cooper correlation, Equation 4 used the average roughness value R_a for the surface roughness parameter. The R-245fa HTCs measured in this study ($T_{sat} = -30^\circ\text{C}$, -40°C , and -50°C) and the R-245fa HTCs from Nagata et al. [13] obtained at higher saturation temperatures ($T_{sat} = 10^\circ\text{C}$, 40°C , and 60°C) were used for the data-correlation process. The fluid molecular mass (M) coefficient was kept at -0.5 as recommended by Cooper because there was insufficient data to evaluate the effect of this parameter on HTCs (i.e., only R-245fa results were used).

The coefficients that provided the best correlation fit to the data were determined to be $C_0 = 50.8$, $C_1 = 0.73$, and $C_2 = -1.02$. Figure 13 plots the correlation-predicted values versus the experimental results. As shown, the majority of the predicted R-245fa results fall within $\pm 20\%$ of the experimental data. The prediction capabilities from the proposed correlation are an improvement over the prediction capabilities of existing correlations for low saturation temperatures below -30°C . Attempts to correlate the HTCs for the microporous-coated samples were not successful because boiling on the microporous surfaces is a more complex process (as compared to boiling on a plain surface). Accurately modeling boiling on coated surfaces would require more detailed models that incorporate the effects of coating porosity, pore size, coating thickness, and coating material.

The modified form of the Zuber CHF [31] equation shown in Equation 5 was used to correlate the CHF values for both the plain and the microporous-coated samples.

$$\frac{q''_{CHF}}{q''_{CHF,Z}} = a P_{red}^b \quad \text{Equation 5}$$

$$q''_{CHF,Z} = (\pi/24) \rho_v^{1/2} h_{lv} [g\sigma(\rho_l - \rho_v)]^{1/4} \quad \text{Equation 6}$$

where q''_{CHF} is the predicted CHF and $q''_{CHF,Z}$ is the Zuber-predicted CHF (Equation 6). In Equation 6, ρ_v is the vapor density, ρ_l is the liquid density, h_{lv} is the latent heat, and σ is the surface tension. Through linear regression, the coefficients were computed to be $a = 0.15$ and $b = -0.35$ for the plain surface and $a = 0.36$ and $b = -0.35$ for the microporous-coated surfaces. The CHF values predicted by Equation 5 are within $\pm 1\%$ of the measured CHF values (Figure 14).

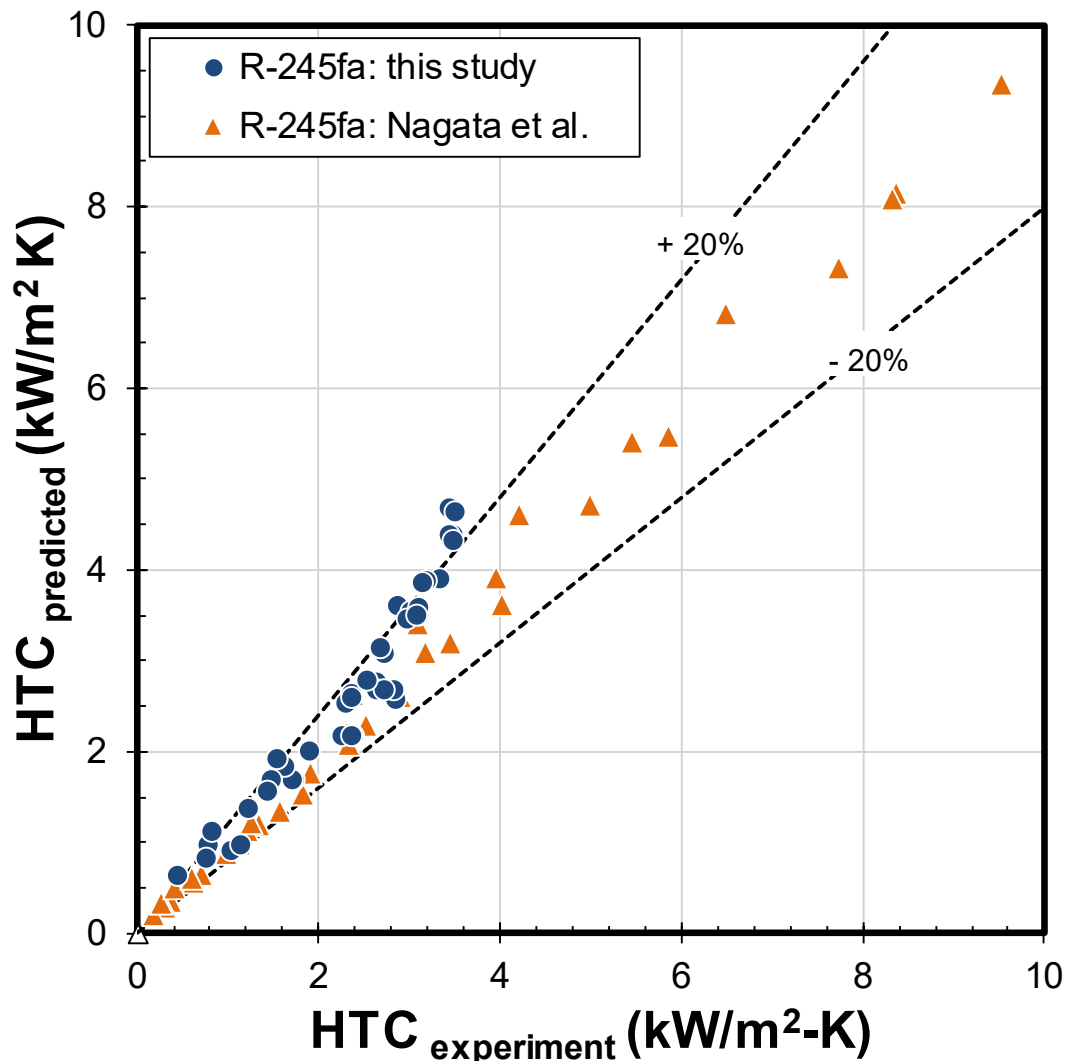


Figure 13. Boiling HTC-predicted values per Equation 4 plotted versus the experimentally obtained values. Reference data source: Nagata et al. [13]

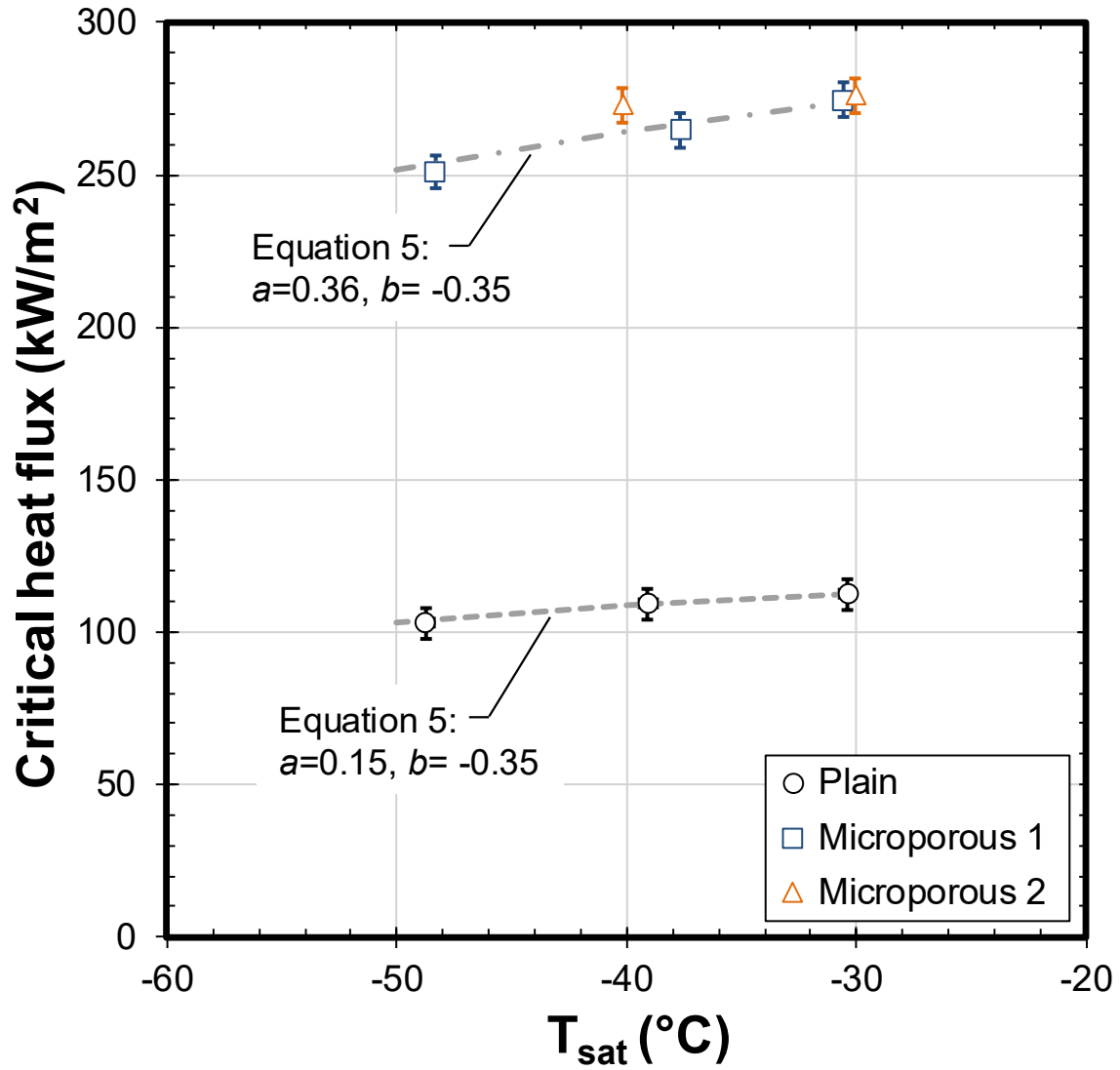


Figure 14. CHF versus T_{sat} for the two microporous-coated samples and the plain sample.

4 Conclusions

Pool boiling experiments were conducted to measure HTC and CHF values for R-245fa at low saturation temperatures ($T_{sat} = -30^{\circ}\text{C}$, -40°C , and -50°C). The effects of two microporous coatings, each fabricated using particles of different sizes, on boiling heat transfer were investigated. The research was prompted by the need to develop efficient methods for pre-cooling hydrogen in fuel cell electric vehicle fueling applications. The major conclusions are summarized below.

- HTC and CHF decreased with decreasing saturation temperatures. Additionally, the HTCs for the plain sample were relatively low for two-phase boiling standards. The low boiling performance is associated with an increase in heated surface vapor coverage (i.e., larger bubble departure diameters and lower departure frequencies) and fewer active nucleation sites at lower saturation temperatures. The use of surface enhancement techniques is recommended to increase boiling heat transfer for low reduced-pressure conditions.
- The two microporous coatings tested produced similar thermal performance. The coatings increased HTCs and CHF values by as much as 460% and 140%, respectively, over the plain surface. The enhancements are associated with increased surface area, increased number of active nucleation sites, increased evaporation, and passive fluid transport via capillary wicking. Surprisingly, boiling incipient superheat was relatively high (as much as 46 K) for the microporous coating samples. Analysis of nucleation phenomena suggests that the use of microporous coatings with larger cavities and pores (as compared to the coatings used in this study) may yield better results for low reduced-pressure conditions (i.e., low saturation temperatures), provide higher HTC, and lower boiling incipient superheat values.
- Available HTC and CHF correlations that provided the best match with experimental results were found to deviate by as much as 48% as compared to experimentally measured values. An HTC correlation was proposed for plain surface cylindrical heaters using R-245fa data at saturation temperatures ranging from -50°C to 60°C . CHF correlations for the plain and microporous cylindrical samples were also developed using the R-245fa CHF results and are applicable for T_{sat} range of -50°C to -30°C . The proposed HTC and CHF correlations were found to be more accurate compared with existing correlations at the low temperatures considered in this study.
- Refrigerant R-245fa was used for this study because it is a non-flammable refrigerant that is commonly used in passive two-phase cooling applications. The downsides of R-245fa are its relatively high global warming potential (GWP = 858 [36]) and very low (sub-ambient) pressure at temperatures of -50°C . The authors recommend future work be conducted to evaluate the use of modern, environmentally friendly (low GWP), and higher-pressure refrigerants such as HFO-1234ze (GWP <1 [36]) or HFO-1234yf (GWP <1 [36]).

5 Nomenclature

| | |
|----------|---|
| D | diameter, m |
| g | gravity, m/s^2 |
| h | heat transfer coefficient, $\text{kW/m}^2 \text{K}$ |
| h_{lv} | latent heat, kJ/kg |

| | |
|-------|--|
| k | thermal conductivity, kW/m K |
| L | length, m |
| P | pressure, MPa |
| q | heat, kW |
| q'' | heat flux, kW/m ² |
| r | radius, m |
| r' | dimensionless radius |
| R_a | surface roughness parameter, μm |
| R_p | Glattungstiefe surface roughness parameter (used in the Copper correlation), μm |
| T | temperature, C or K |

Greek Symbols

| | |
|----------|----------------------------|
| μ | viscosity, Pa s |
| ρ | density, kg/m ³ |
| σ | surface tension, N/m |

Subscripts

| | |
|-------|--|
| b | bubble |
| c | critical (e.g., critical pressure) |
| CHF | critical heat flux, kW/m ² |
| l | liquid |
| red | reduced (e.g., reduced pressure, P/P_c) |
| sat | saturated |
| sys | system |
| v | vapor |
| w | wall |
| Z | Zuber correlation |

6 Acknowledgments

The authors would like to thank the NREL Laboratory Directed Research and Development Program for financial support of this work. This work was authored by the Alliance for Sustainable Energy, LLC, the manager and operator of the National Renewable Energy Laboratory for the U.S. Department of Energy (DOE) under Contract No. DE-AC36-08GO28308. The views expressed in the article do not necessarily represent the views of the DOE or the U.S. Government. The U.S. Government retains and the publisher, by accepting the article for publication, acknowledges that the U.S. Government retains a nonexclusive, paid-up, irrevocable, worldwide license to publish or reproduce the published form of this work, or allow others to do so, for U.S. Government purposes.

7 References

- [1] 2017, "Hydrogen Storage Tech Team Roadmap" [Online]. Available: https://energy.gov/sites/prod/files/2017/08/f36/hstt_roadmap_July2017.pdf. [Accessed: 16-Jan-2018].
- [2] Rainey, K. N., You, S. M., and Lee, S., 2003, "Effect of Pressure, Subcooling, and Dissolved Gas on Pool Boiling Heat Transfer from Microporous, Square Pin-Finned Surfaces in FC-72," *Int. J. Heat Mass Transf.*, **46**(1), pp. 23–35.
- [3] Cichelli, M. T., and Bonilla, C. F., 1945, "Heat Transfer to Liquids Boiling under Pressure," *Trans. Am. Inst. Chem. Eng.*, **41**(6), pp. 755–787.
- [4] Moreno, G., Narumanchi, S., and King, C., 2013, "Pool Boiling Heat Transfer Characteristics of HFO-1234yf on Plain and Microporous-Enhanced Surfaces," *J. Heat Transf.*, **135**(11), p. 111014.
- [5] Moreno, G., Jeffers, J. R., and Narumanchi, S., 2014, "Effects of Pressure and a Microporous Coating on HFC-245fa Pool Boiling Heat Transfer," *J. Heat Transf.*, **136**(10), pp. 101502–101502.
- [6] Lee, J., and Mudawar, I., 2008, "Fluid Flow and Heat Transfer Characteristics of Low Temperature Two-Phase Micro-Channel Heat Sinks—Part 1: Experimental Methods and Flow Visualization Results," *Int. J. Heat Mass Transf.*, **51**(17), pp. 4315–4326.
- [7] Lee, J., and Mudawar, I., 2008, "Fluid Flow and Heat Transfer Characteristics of Low Temperature Two-Phase Micro-Channel Heat Sinks—Part 2. Subcooled Boiling Pressure Drop and Heat Transfer," *Int. J. Heat Mass Transf.*, **51**(17), pp. 4327–4341.
- [8] de Rossi, F., Mauro, A. W., and Rosato, A., 2009, "Local Heat Transfer Coefficients and Pressure Gradients for R-134a during Flow Boiling at Temperatures between -9°C and $+20^{\circ}\text{C}$," *Energy Convers. Manag.*, **50**(7), pp. 1714–1721.
- [9] Wattelet, J. P., Chato, J.C., Souza, A. L., and Christoffersen, B. R., 1994, "Evaporative Characteristics of R-12, R134a, and a Mixture at Low Mass Fluxes," *ASHRAE Trans.*, **100**(1).
- [10] Thome, J. R., 1996, "Boiling of New Refrigerants: A State-of-the-Art Review," *Int. J. Refrig.*, **19**(7), pp. 435–457.
- [11] Ribatski, G., and Jabardo, J. M. S., 2003, "Experimental Study of Nucleate Boiling of Halocarbon Refrigerants on Cylindrical Surfaces," *Int. J. Heat Mass Transf.*, **46**(23), pp. 4439–4451.
- [12] Webb, R. L., and Pais, C., 1992, "Nucleate Pool Boiling Data for Five Refrigerants on Plain, Integral-Fin and Enhanced Tube Geometries," *Int. J. Heat Mass Transf.*, **35**(8), pp. 1893–1904.
- [13] Nagata, R., Kondou, C., and Koyama, S., 2016, "Comparative Assessment of Condensation and Pool Boiling Heat Transfer on Horizontal Plain Single Tubes for R1234ze(E), R1234ze(Z), and R1233zd(E)," *Int. J. Refrig.*, **63**(Supplement C), pp. 157–170.

- [14] van Rooyen, E., and Thome, J. R., 2013, "Pool Boiling Data and Prediction Method for Enhanced Boiling Tubes with R-134a, R-236fa and R-1234ze(E)," *Int. J. Refrig.*, **36**(2), pp. 447–455.
- [15] Gorgy, E., 2016, "Nucleate Boiling of Low GWP Refrigerants on Highly Enhanced Tube Surface," *Int. J. Heat Mass Transf.*, **96**(Supplement C), pp. 660–666.
- [16] Dewangan, A. K., Kumar, A., and Kumar, R., 2016, "Nucleate Boiling of Pure and Quasi-Azeotropic Refrigerants from Copper Coated Surfaces," *Appl. Therm. Eng.*, **94**(Supplement C), pp. 395–403.
- [17] Hsieh, S.-S., and Weng, C.-J., 1997, "Nucleate Pool Boiling from Coated Surfaces in Saturated R-134a and R-407c," *Int. J. Heat Mass Transf.*, **40**(3), pp. 519–532.
- [18] Ji, W.-T., Qu, Z.-G., Li, Z.-Y., Guo, J.-F., Zhang, D.-C., and Tao, W.-Q., 2011, "Pool Boiling Heat Transfer of R134a on Single Horizontal Tube Surfaces Sintered with Open-Celled Copper Foam," *Int. J. Therm. Sci.*, **50**(11), pp. 2248–2255.
- [19] Carey, V. P., 1992, *Liquid-Vapor Phase Change Phenomena*, Taylor & Francis, Hebron, KY.
- [20] Bakhru, N., and Lienhard, J. H., 1971, "Boiling from Small Cylinders," *Int J Heat Mass Transf.*, **15**, pp. 2011–2025.
- [21] Raj, R., and Kim, J., 2010, "Heater Size and Gravity Based Pool Boiling Regime Map: Transition Criteria Between Buoyancy and Surface Tension Dominated Boiling," *J. Heat Transf.*, **132**(9), pp. 091503-091503–10.
- [22] National Institute of Standards and Technology, 2017, "Thermophysical Properties of Fluid Systems" [Online]. Available: <http://webbook.nist.gov/chemistry/fluid/>. [Accessed: 13-Nov-2017].
- [23] Lau, J. H., and Pao, Y.-H., 1997, *Solder Joint Reliability of BGA, CSP, Flip Chip, and Fine Pitch SMT Assemblies*, McGraw-Hill Professional Publishing.
- [24] Dieck, R. H., 2007, *Measurement Uncertainty: Methods and Applications*, ISA, Research Triangle Park, NC, USA.
- [25] Cooper, M. G., 1984, "Saturation Nucleate Pool Boiling - A Simple Correlation," *1st U.K. National Conference on Heat Transfer*, Pergamon Press, pp. 785–792.
- [26] Jung, D., Lee, H., Bae, D., and Oho, S., 2004, "Nucleate Boiling Heat Transfer Coefficients of Flammable Refrigerants," *Int. J. Refrig.*, **27**(4), pp. 409–414.
- [27] Gorenflo, D., Baumhögger, E., Herres, G., and Kotthoff, S., 2014, "Prediction Methods for Pool Boiling Heat Transfer: A State-of-the-Art Review," *Int. J. Refrig.*, **43**(Supplement C), pp. 203–226.
- [28] Jones, B. J., McHale, J. P., and Garimella, S. V., 2009, "The Influence of Surface Roughness on Nucleate Pool Boiling Heat Transfer," *J. Heat Transf.*, **131**(12), pp. 121009-121009–14.

- [29] Lienhard, J. H., and Dhir, V. K., 1973, "Hydrodynamic Prediction of Peak Pool-Boiling Heat Fluxes from Finite Bodies," *J. Heat Transf.*, **95**(2), pp. 152–158.
- [30] Sun, K.-H., and Lienhard, J. H., 1970, "The Peak Pool Boiling Heat Flux on Horizontal Cylinders," *Int. J. Heat Mass Transf.*, **13**(9), pp. 1425–1439.
- [31] Zuber, N., 1959, "Hydrodynamic Aspects of Boiling Heat Transfer," *Phys. Math.*, **AEC Report No. AECU-4439**.
- [32] Li, C., and Peterson, G. P., 2007, "Parametric Study of Pool Boiling on Horizontal Highly Conductive Microporous Coated Surfaces," *J. Heat Transf.*, **129**(11), pp. 1465–1475.
- [33] Ha, M., and Graham, S., 2017, "Pool Boiling Characteristics and Critical Heat Flux Mechanisms of Microporous Surfaces and Enhancement through Structural Modification," *Appl. Phys. Lett.*, **111**(9), p. 091601.
- [34] You, S. M., Simon, T. W., Bar-Cohen, A., and Tong, W., 1990, "Experimental Investigation of Nucleate Boiling Incipience with a Highly-Wetting Dielectric Fluid (R-113)," *Int. J. Heat Mass Transf.*, **33**(1), pp. 105–117.
- [35] You, S. M., Bar-Cohen, A., and Simon, T. W., 1990, "Boiling Incipience and Nucleate Boiling Heat Transfer of Highly Wetting Dielectric Fluids from Electronic Materials," *IEEE Trans. Compon. Hybrids Manuf. Technol.*, **13**(4), pp. 1032–1039.
- [36] Stocker, T., 2014, *Climate Change 2013: The Physical Science Basis: Working Group I Contribution to the Fifth Assessment Report of the Intergovernmental Panel on Climate Change*, Cambridge University Press.